Journal of
Materials Chemistry C

PAPER

View Article Online
View Journal

Cite this: DOI: 10.1039/c6tc03623f

Laser annealing of electrodeposited $CuInSe_2$ semiconductor precursors: experiment and modeling†

H. J. Meadows,[a] S. Misra,[b] B. J. Simonds,[c] M. Kurihara,[a] T. Schuler,[a] V. Reis-Adonis,[a] A. Bhatia,[d] M. A. Scarpulla[bd] and P. J. Dale*[a]

Laser annealing can reduce the annealing time required to form $Cu(In,Ga)(S,Se)_2$ (CIGSe) thin films for use in thin film photovoltaics to a single second timescale, if not faster. In this work, we use microstructural characterization coupled with modeling of the optical and thermal properties to understand the laser annealing of three types of electrodeposited precursor stacks for the CIGSe parent compound $CuInSe_2$. The precursor films are: stacked elemental layers Cu/In/Se, stacked binary selenides $In_2Se_3/Cu_{2-x}Se$, and a single layer of coelectrodeposited Cu–In–Se. Conceptually, these stacks are ordered in terms of decreasing stored chemical and interfacial potential free energy, consideration of which predicts that the formation of large grained $CuInSe_2$ from the stacked elemental layers would be the most exothermic and thus most rapid process. However we find that microstructural details of the electrodeposited films such as void fraction present in the stacked binary selenides dramatically alter the heat and mass flow. Additionally, modeling of the optical absorption within the elemental stacked precursor suggests extremely localized heating at the In/Se interface resulting in significant Se loss. Despite its lower chemical potential energy, the coelectrodeposited $CuInSe_2$ precursor's more uniform optical absorption of near-bandgap light coupled with its compact, low void fraction microstructure of nano-sized grains results in the most optimal recrystallization and compositional homogenization *via* interdiffusion. Furthermore this annealed layer formed a working device with a short circuit current density of 23 mA cm^{-2}. This combined modeling and experimental investigation underscores the need to consider practical micro- and nanostructure-dependent properties as well as the optical absorption and not simply thermodynamics when designing accelerated two step deposition and annealing processes for compound semiconductors.

Received 22nd August 2016,
Accepted 24th November 2016

DOI: 10.1039/c6tc03623f

www.rsc.org/MaterialsC

Introduction

$Cu(In,Ga)(S,Se)_2$ (CIGSe) based devices have the highest light to electrical power conversion efficiency of all thin film polycrystalline photovoltaics (TFPV, 22.6%[1]). Industrially, the CIGSe semiconductor is produced by vacuum deposition of thin film precursor multilayers followed by annealing in chalcogen atmospheres for tens of minutes to hours.[2,3] In order to increase the competitiveness of TFPV modules, module production cost per Watt generating capacity must be further reduced. This is achievable by increasing module power conversion efficiency or by decreasing the direct (*i.e.* raw materials and energy) and indirect (*i.e.* equipment and interest) costs. Both costs are reduced if the production facility's throughput is increased. Electrodeposition is an alternative synthesis method to vacuum deposition methods for CIGSe precursor layers and has production advantages that are currently used commercially such as near-unity material utilization, simplicity, low power consumption, and rapid growth rates.[4] Laser annealing is an alternative heating method to resistive element furnaces and has the advantage of rapidly heating the active layers to temperatures above the mechanical melting point of the underlying substrate. Previously laser annealing has been used to crystallize silicon that made solar cells with a power conversion efficiency of 11%,[5] and anneal TiO_2 nanoparticles for dye sensitized solar cells giving an efficiency of 7.1%.[6] It has also been used to modify already synthesized CIGSe layers. Non-melting pulsed laser annealing of the semiconductor increased carrier mobility and lifetime improving the device

[a] *Physics and Materials Science Research Unit, University of Luxembourg, 41 rue du Brill, Belvaux, Luxembourg. E-mail: Phillip.dale@uni.lu*
[b] *Electrical and Computer Engineering, University of Utah, Salt Lake City, Utah, USA*
[c] *National Institute of Standards and Technology (NIST), Boulder, Colorado, USA*
[d] *Materials Science and Engineering, University of Utah, Salt Lake City, Utah, USA*
† Electronic supplementary information (ESI) available: Free energy calculation, spatial temperature distribution as a function of time video and maximum annealing temperature as a function of beam position on the precursor substrate. See DOI: 10.1039/c6tc03623f

efficiency from near 8% up to 13%.[7] In this combined modeling and experimental study we investigate the combination of electrodeposition and high-intensity infrared laser annealing for conversion of different types of electrodeposited precursors into the desired CIGSe phase opening a path to high speed semiconductor synthesis.

Industrial fabrication of CIGSe thin films involves the deposition of the constituent elements in one or more precursor layers onto a Mo substrate at low temperature and their subsequent reaction into the chalcopyrite phase at high temperature. The best laboratory device power conversion efficiency for CIGSe based on this two-step process is 20.9% achieved by annealing a vacuum deposited metallic precursor in a chalcogen containing atmosphere.[8] This high efficiency is only possible by carefully matching the precursor properties and the annealing routine to one another. In other words, no one annealing routine will produce the same quality semiconductor layer for different types of precursor. In this work we aim to investigate which type of CIGSe precursor is most suitable for laser annealing times of a single second. Precursors can consist of elemental layers, binary chalcogenide layers, or consist of all the elements intimately mixed, or some combination of the above.

Previously, laser annealing of precursors to synthesize CIGSe semiconductor has been reported. Dhage *et al.* reported the sintering of CIGSe nanoparticle precursors using a fibre coupled diode laser with a 200 W beam scanned at 125 mm s^{-1} to form crystalline layers.[9] Laude *et al.* laser annealed 100 nm thick precursor films consisting of thin layers of Cu, In and Se deposited on glass or on NaCl crystals.[10,11] Optical absorbance measurements suggested that the resulting films had a measurable band gap of 0.95 eV, consistent with copper poor $CuInSe_2$. Bhattacharyya *et al.* laser annealed In/Cu/Se stacks on glass substrates using an Argon ion laser.[12] They found that increasing laser power from 260 W cm^{-2} to 1300 W cm^{-2} reduced the presence of CuIn, In_2Se_3, and CuSe secondary phases to undetectable levels as measured by X-ray diffraction. Jost *et al.* laser annealed coelectrodeposited $CuInSe_2$ using a 1064 nm irradiation and produced a crystalline film.[13] However, since the laser power was $>10^4$ W cm^{-2} the $CuInSe_2$ layer melted and dewetted from the substrate making it unsuitable for use as a solar cell absorber layer. All the reports described so far used different precursors, and all use different laser annealing conditions. These differences in both precursor and laser annealing conditions makes comparison between the studies difficult, and therefore it is also unclear which type of precursor structure is best to use. Also none of the reviewed literature so far reports on any of the semiconductor properties that actually determine solar cell performance such as doping, minority carrier mobility or lifetime, *etc.*, making it hard to establish the quality of the produced films.

Some of the current authors have reported on the laser annealing of coelectrodeposited $CuInSe_2$.[14] Here a micron thick precursor was annealed with a 1064 nm continuous wave laser. It was found that a single second of annealing was sufficient to produce single phase $CuInSe_2$ and to remove elemental gradients through the depth of the film. The crystallite coherence length of the layers improved with increasing power and time. The laser annealed $CuInSe_2$ layers were found to be p-type doped semiconductors and showed weak photoluminescence, an indicator of the desired radiative recombination. However, when the layers were finalized into device structures they did not produce any power. More recently, we have shown that a large selenium overpressure is required during laser annealing since without it, selenium is lost from the layer during the annealing process.[15] Higher partial pressures of selenium led to improved crystal coherence length within the film and increased photoluminescence yield. Similar to laser annealing is flash lamp annealing and Stolle *et al.* reported a 1.25% efficient $CuInSe_2$ device with the absorber layer consisting of FLA $CuInSe_2$ quantum dots annealed at 873 K.[16] Given that single-phase CIGSe material yielding high power conversion efficiency is possible by resistive thermal annealing, two research questions are (1) why does it fail for laser annealing and related methods, and (2) more broadly which type of precursor structure is most suitable for laser annealing?

We investigate the above questions by examining the quality of $CuInSe_2$ (CISe) semiconductor produced from three different types of electrodeposited precursors annealed under the same laser conditions. CISe is chosen over CIGSe to reduce the number of experimental variables. The three precursors types are (a) stacked elemental layers of the individual elements, Cu, In and Se, (b) the stacked binary metal selenides, In_2Se_3 and $Cu_{2-x}Se$, and (c) all the elements Cu–In–Se codeposited in a single step (see Fig. 1). These precursors vary in their optical properties, chemical potential energy and microstructure, each of which could be important for the successful synthesis of an optimized polycrystalline chalcopyrite thin film after single second laser annealing. Broadly speaking the optical properties

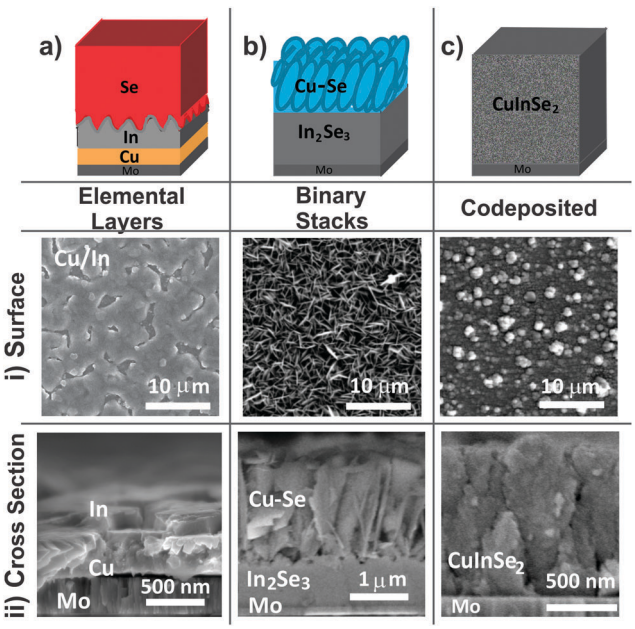

Fig. 1 Schematic representations of electrodeposited precursors: (a) Cu/In/Se stacked elemental layers, (b) $In_2Se_3/Cu_{2-x}Se$ binary selenide stacks, (c) co-deposited $CuInSe_2$. SEM micrographs of (i) surface and (ii) the cross sectional view of each of the samples (a–c). Note that (ai) and (ii) show Cu/In prior to Se capping.

will affect the temperature that the precursor reaches, the chemical potential energy and reaction pathways will govern the temperature that is required for the reaction kinetics to be sufficient, and the microstructure will affect how quickly and how far elements must diffuse. Each of these is considered below.

Resistive thermal annealing heats the precursor to thermal equilibrium by blackbody radiation and convection from the vapor phase environment whereas single second laser annealing requires the specific absorption of a unique wavelength to cause sub-second heating. The temperature trajectory that the precursor experiences depends on its optical properties, the irradiation wavelength and flux of the laser, as well as the specific heat capacity and thermal conductivity of the precursor layer(s). Superior optoelectronic properties, such as long minority carrier lifetimes in inorganic semiconductors, are typically achieved by heating them to temperatures of one half to two thirds of their melting points (or homologous temperature $\sim$0.5–0.7). CIGSe is commonly processed at temperatures between 723–873 K[17] corresponding to a homologous temperature of $\sim$0.6–0.7. As the explicit aim of this work is to heat for only one second, probably higher homologous temperatures are required. Upper limits on temperature are set by sample failure modes such as delamination, thermal shock to glass substrates, warping of metal substrates, and dewetting of a molten film.

The chemical reactivity of a precursor is governed by its overall Gibbs free energy of reaction, and estimates of these are tabulated in Table 1 for all the precursor types. The stacked elemental precursor has a considerably more negative free energy of reaction than the other precursors due to the selenide bond formation that occurs. We estimate that the codeposited $CuInSe_2$ precursor has a small free energy of reaction as depth profiles of the layers indicated the presence of copper and binary selenides, in addition to the $CuInSe_2$ phase (ESI†). From these estimates we conclude that the stacked elemental layers should be the most reactive. Despite this expected higher reactivity, CISe formation is observed at similar temperatures for the stacked elemental layers and binary chalcogenide stacks, whilst the codeposited precursor already contains a significant fraction of CISe as electrodeposited at 293 K. *In situ* and *ex situ* X-ray diffraction shows that elemental stacks can be completely reacted at a relatively low 723 K after only 1.5 min. The binary stacks however are incompletely reacted at this temperature after 30 min[18] and require an annealing temperature of 823 K to be fully reacted in this time. The codeposited sample, despite containing a significant CISe fraction, requires annealing at 723 K for 30 min. From these considerations it would appear that the elemental stack requires the lowest processing temperature and the binary stack the highest. Additionally, nano-crystalline precursors will gain negative free energy from the excess grain boundary energy while stacked elemental precursors also have free energy relating to the interfaces. More negative formation energies may stimulate the formation of larger grains and superior optoelectronic properties in the absorber by increasing driving forces for reactions. This framework is consistent with power conversion efficiencies achieved in devices fabricated from electrodeposited and annealed $CuInSe_2$ absorbers: 9% for elemental layers and 7.5% for coelectrodeposited $CuInSe_2$ using the same annealing routine.[19]

As a last point of consideration, microstructure may also be important. The three different precursors have different numbers of chemical phases and thus interfaces. Two compact phases separated by a single interface may diffuse into one another quickly, but a porous layer on top of a compact phase has less surface area through which the two phases may diffuse into one another and thus requires a relatively longer annealing time. Nano-crystalline samples contain by definition many grain boundaries which are expected to accelerate the rate of diffusion of elements compared to bulk diffusion.

Therefore, this work considers the interaction between the laser beam and three different electrodeposited precursors in order to select the most suitable precursor structure for laser annealing. Firstly, each precursor is characterized to determine its phases and microstructure. Secondly, the optical coefficients of the precursor materials are considered and their effect on the absorption of the laser energy. The dissipation of laser energy through each precursor stack is simulated and then this is converted into heat flow in order to obtain a time-temperature profile. Finally these profiles are combined with empirical experimental observations of the structure, phases and level of crystallinity of the laser annealed absorber layers in order to understand the annealing process. Using this approach, and despite the fact that stacked elemental layers appear to be optimal for traditional furnace annealing, the most suitable precursor for laser annealing is found to be the coelectrodeposited, nanocrystalline precursor. While the other two precursor types paired with this ultra-fast annealing could not result in CISe formation, the suitability of co-electrodeposited precursors is demonstrated by the synthesis of functioning solar cell devices.

Methods

All precursor types were electrodeposited onto substrates comprising 3 mm-thick glass sputter coated with a 400 nm

Table 1 Free energy of reaction (ΔG) at 273 K, literature CISe formation temperatures, and minimum temperatures and times for complete CISe formation, for all precursor types. The free energy calculation will vary with temperature, but the relative ordering of the samples is not expected to vary

Precursor type	ΔG (kJ mol^{-1})	Temperature that CISe formation starts (K)	Minimum temperature that CISe formation is completed (K)	Minimum annealing time (min)
Elemental stack Cu/In/Se	−241 to −282[20,21]	643[22]	723[22]	1.5[22]
Binary stack $In_2Se_3/Cu_{2-x}Se$	−9 to −50[21]	623[18]	823[18]	30[18]
Co-deposited $CuInSe_2$	−6 to −11 [this work]	293	723[23]	30[23]

layer of Mo. All depositions were carried out in a three electrode cell, with the Mo-coated glass suspended horizontally to form the working electrode while a Pt foil and Ag/AgCl electrode formed the counter and reference electrodes respectively. The depositions were controlled potentiostatically (unless otherwise stated). The duration of each deposition was determined with respect to the total charge passed in order to give a near stoichiometric composition in the final $CuInSe_2$ layer and to yield a 1–2 μm thick $CuInSe_2$ absorber layer after laser processing. For Cu/In/Se precursors, initially a thin layer of Cu was deposited from an alkaline bath, as detailed in ref. 24, to provide a nucleation layer on the Mo. A second Cu layer was deposited on top from an acidic bath, using a galvanostatically controlled deposition (current density 5 mA cm^{-2}), as detailed in ref. 25 in order to give an overall, smooth, homogeneous layer. Indium was then immediately deposited onto the Cu layer using a plating solution (pH 3) consisting of 0.26 M $InCl_3$ (Alfa Aesar 99.99%), 2.3 M sulfamic acid (Sigma Aldrich 99.5%), 2.0 M NaCl (Sigma Aldrich 98%), 0.04 M D-glucose (Sigma Aldrich) and 0.02 M triethylamine (Sigma Aldrich). Initially a potential of −1.3 V was applied for 0.1 s to form nucleation centers followed by deposition at −0.97 V. Finally, excess of Se was evaporated onto the Cu/In film surface using the technique given in ref. 14. $In_2Se_3/Cu_{2-x}Se$ samples were formed *via* the method described in ref. 26. CISe was deposited from a bath containing Cu, In and Se using the method described in ref. 14. Additional $CuCl_2$ was added to the deposition bath to give a film composition close to stoichiometry (Cu/In = 0.91–0.99).

Annealing was carried out using a continuous wave (CW) Nd:YAG solid state laser (λ = 1064 nm). The beam was Gaussian shaped with a full width half maximum intensity of 1.8 mm. The beam was collimated and passed through a 2 × 2 mm aperture with a laser flux 150 W cm^{-2} measured after the aperture. Each sample was affixed into a small volume annealing chamber with a quartz window, which was purged with Ar prior to annealing. An automated *x*–*y* stage was used to scan the sample through the laser beam with 2 mm s^{-1} scan rate, giving a dwell time ≈1 s and therefore a total energy of 6 J on any 2 × 2 mm spot. The beam was scanned horizontally from one side to the other side and then vertically translated by 1.8 mm before being horizontally scanned again in the opposite direction. These conditions were considered suitable to achieve a fairly even irradiant energy distribution over the centimeter sized samples. This consideration was based on examining the microstructure, chemical gradients, and the photoluminescence yield across the width of a single pass of the laser beam on a CISe codeposited precursor.[27]

The time-dependent heat flow and temperatures in the samples were computed using the finite element method (FEM) implemented in COMSOL Multiphysics v.4.4. The simulation included heat diffusion in all layers (including the much thicker glass) and the boundary conditions on both the film side and back side of the glass substrate were diffusion and natural convection to air at 300 K. For computational efficiency, the analytically-computed optical absorption profiles for all samples were used to define a depth-dependent heat source in the FEM calculations. Assuming normal incidence and non-magnetic materials, the electric field magnitude $E(x, t)$ within each precursor stack layer may be expressed as a linear sum of forward and backward propagating plane waves (with A and B coefficients, which may be complex, determined for each stack):

$$E(x, t) = E_0 e^{-i\omega t}(Ae^{-ikx} + Be^{-ikx}) \quad (1)$$

The electric field, Poynting vector, and absorbed power were computed analytically throughout the stacks using a transfer matrix approach. Within each layer, defined for the optical problem by its thickness and complex refractive index N, the time-averaged depth profile of power absorbed from the electric field $E(x, t)$ and converted into heat (with units of power/length^3) can be shown to equal:

$$\bar{P}_{abs}(x) = \mathrm{Re}\left[\frac{\alpha n c \varepsilon_0 |E_0|^2}{2}\left\{A^2 e^{-\alpha x} + \frac{2nAB}{k}\sin\left(\frac{4\pi n x}{\lambda}\right) - B^2 e^{\alpha x}\right\}\right] \quad (2)$$

in which λ is the vacuum wavelength, $N = n + ik$ is the complex refractive index, $\alpha = 4\pi k/\lambda$ is the absorption coefficient, c is the speed of light, and ε_0 is the vacuum permittivity. For both the heat flow and optical problems, we simulate the entire sample including the substrate which is approximately three orders of magnitude thicker than the thin film(s). A non-uniform mesh was generated to give high spatial resolution in the thin film region while much larger elements were used in the glass for computational efficiency. Consideration of the glass is critical for the heat flow problem as the heating of the glass substrate results in transient heat flow until steady-state is established at a typical time we find both experimentally and computationally to be on the order of 30 s (thus these experiments were all carried out in the transient regime). For the heat flow problem, the samples were modeled in 3D using a 1 × 1 cm^2 lateral area with a 2 × 2 mm^2 area in the center over which 150 W cm^{-2} of uniform laser power was incident for 1 s and then turned off. Although we are only simulating a stationary beam as opposed to the scanning beam used for experiments, the temperatures given are representative of the equilibrium values achieved over the majority of the sample while the scanned beam is away from the sample edges. In order to validate the calculated time temperature profiles we measured the temperature change of the back of the glass substrate during and after laser irradiation with a thermocouple. A good agreement between the experimental and calculated temperature profiles was found, and the details of which are given in the ESI.†

Analysis of the morphology and composition of the precursor and laser annealed samples was carried out using scanning electron microscopy (SEM) and energy dispersive X-ray spectroscopy (EDX) on a combined Hitachi SU 70 system. X-ray diffraction measurements were made using a Panalytical X'Pert Pro system with Cu K_α radiation and θ–2θ Bragg–Brentano geometry. Raman measurements were made on a Wittec Micro Raman confocal microscope, with a 532 nm laser at a power of 5 mW and beam size ≈1.3 μm.

Devices were formed by chemical bath deposited CdS (50 nm), sputtering i-ZnO (40 nm)/ZnO:Al (370 nm) layers and

scribing 0.1 cm^2 cells (3 mm × 3 mm) onto the sample. Current–voltage under AM1.5 illumination and external quantum efficiency measurements were carried out at room temperature.

Results and discussion

1. Characterizing electrodeposited precursors

This paper investigates which electrodeposited precursor is most suitable to give a CISe absorber layer with desirable qualities for a photovoltaic device using transient laser annealing for 1 s (*i.e.* below the timescales within which a steady state temperature is reached within the layers). The three precursor structures tested were: stacked elemental layers, binary selenide stacks and a single layer of coelectrodeposited Cu, In and Se. A schematic of each precursor along with their surface and cross sectional appearance in SEM is presented in Fig. 1. The appearance and morphology of each of the precursors shown in Fig. 1 is very different. Metallic stacks of Cu/In/Se, have a compact, smooth layer of Cu visible in the cross section image (Fig. 1aii), onto which the In deposits as an island-like structure (i). This results in a film with varying thickness over which the evaporated Se forms a smooth layer (not shown in SEM micrographs for clarity). The red color of this Se layer indicates its amorphous structure. $In_2Se_3/Cu_{2-x}Se$ precursors have a needle-like appearance when viewed from the surface (Fig. 1bi). To ascertain their structure, the cross sectional image (ii) is analyzed, in which $Cu_{2-x}Se$ is seen to form large platelets approximately 50 nm thick on top of a smooth, flat layer of In_2Se_3, as represented in the schematic (b). Due to the low density of the $Cu_{2-x}Se$ layer, the actual layer thickness is approximately 1800 nm, much greater than the expected 800 nm thus we can conclude that the layer consists of 56% void space. For optical and thermal modeling, an effective medium mixture of air and $Cu_{2-x}Se$ was assumed (*i.e.* linear mixing of properties for voids and $Cu_{2-x}Se$). The codeposited films (Fig. 1c) consist of a compact layer of nanometer dimensioned grains (ii). Surface obtrusions of around 1 μm diameter are observed in the surface view (i). In the next section the optical and thermal properties of these three precursors will be used in order to model the laser power absorption and the time-temperature trajectories of the samples during annealing.

2. Modeling energy absorption and temperature profiles

The interaction between laser beam and each precursor is governed by the optical coefficients of the component materials at the wavelength of λ = 1064 nm. Table 2 gives the optical constants for the relevant materials under study.

The optical coefficients given in Table 2 are briefly interpreted. For Cu/In/Se precursors, whilst Se forms the surface layer of the stack, Se is assumed to have $k = 0$, and thus $\alpha = 4\pi k/\lambda = 0$, meaning the radiation passes unabsorbed through this layer. In contrast, the In layer below has $\alpha = 1.2 \times 10^6$ cm^{-1}, the largest value of the presented materials. As the penetration depth (distance to which the irradiation is attenuated to $1/e$ of its incident intensity) is the inverse of the absorption coefficient, then the majority of the laser energy will be absorbed within 8 nm of In and not reach the Cu layer underneath. Conversely, with $\alpha = 1.8 \times 10^4$ cm^{-1}, CISe has the lowest absorption coefficient and the incident beam is expected to penetrate >400 nm into the film. Due to the multiple reflections within the CISe layer which result from this weak coupling with the laser radiation,[44] the distribution of power absorption within each of the precursor structures was accurately established using FEM.

Fig. 2a–c illustrates the resulting power dissipation through the depth of the precursors and thus initial heat generation profile from the absorption of the laser beam in each precursor. The total power dissipated in the precursors is equal to the area under the curves. As predicted from the optical constants in Table 1, there is no absorption of the laser beam by the surface Se layer of Cu/In/Se precursor (Fig. 2a) and the laser beam power is dissipated within a narrow region at the surface of the In metal, which absorbs only 16% of the irradiation, since most is reflected. This spike in energy would result in heating localized at the In/Se interface. This would vaporize the volatile Se nearest the In interface and perhaps cause the whole Se layer to lift off. Loss of Se by vaporization or lift off would make it unavailable for reaction with the metals. The calculated peak temperature of the Cu/In/Se stack is around 473 K (Fig. 2d – see ESI† for spatially resolved temperature distribution), which is below even the temperature where CISe formation is observed to start (Table 1). Thus for the combined reasons of Se loss and low annealing temperature minimal CISe formation is expected from the stacked elemental layers. The lower temperature could not be addressed simply by increasing the laser power – this would exacerbate the Se loss issues.

In the $In_2Se_3/Cu_{2-x}Se$ binary selenide precursor (Fig. 2b) the incident beam is modelled for porous and compact layers of $Cu_{2-x}Se$. In both cases the beam penetrates to a greater depth than within the In layer (Fig. 2a), as would be expected from the

Table 2 Optical and thermal coefficients of the investigated materials. n, the refraction index, k, the extinction coefficient and α, the absorption coefficient at λ = 1064 nm (1.17 eV). ρ is the density, K is the thermal conductivity, and C_p is the specific heat capacity. For $Cu_{2-x}Se$, the properties of the bulk phase are listed, however effective properties of a $Cu_{2-x}Se$/void mixture were used in some calculations

Property	Glass	Mo[28]	Se[29]	In[30]	Cu[31]	In_2Se_3[32]	Cu_2Se[33]	$CuInSe_2$[34]
n	1.5	2.4	2.8	1.8	0.38	3.2	3.4	3.1
k	0	4.4	0	8.4	7.1	0.3	1.2	0.2
α_{1064nm} ($\times 10^4$ cm^{-1})	0	52	0	120	84	3.5	14	1.8
ρ (g cm^{-3})	2.4	10.2	4.39[35]	7.31[35]	8.96[35]	5.8	6.8[36]	5.77[37]
K (W cm^{-1} K^{-1})	0.009	1.38[35]	0.005[35]	0.818[38]	0.401[35]	0.013[39]	0.01[40]	0.086[41]
C_p (J g^{-1} K^{-1})	0.880	0.251[35]	0.318[42]	0.233[35]	0.386[35]	0.324[43]	0.356[37]	0.300[41]

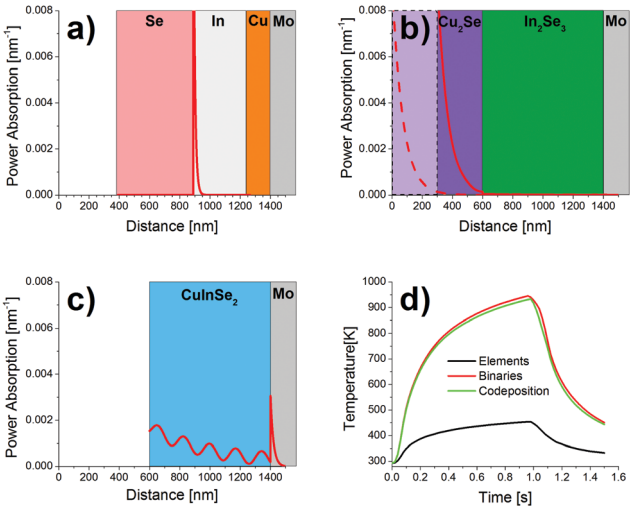

Fig. 2 (a)–(c) Representative optical absorption calculations for (respectively) stacked elemental layers Cu/In/Se, stacked binaries $In_2Se_3/Cu_{2-x}Se$, and coelectrodeposited ternary Cu–In–Se. (b) Dashed and filled line represent absorption in porous (thicker layer as indicated) and compact $Cu_{2-x}Se$ respectively (d) calculated time evolution of temperature in the precursor layers for 1 s laser exposure at 150 W cm^{-2}. The binary layered and ternary co-deposited layers precursors achieve much higher temperatures than the stacked elemental precursor (assuming no absorption in the Se). In all cases, for all but the shortest times, the precursor stacks are nearly isothermal, whereas the glass substrate is heated transiently (because of the much lower thermal diffusivity of glass).

order of magnitude difference in absorption coefficients of Cu_2Se (assumed to be the dominant phase of this layer) and In (1.4×10^5 cm^{-1} compared to 1.2×10^6 cm^{-1} respectively). However, even in the porous case, the vast majority of the beam power is dissipated within the $Cu_{2-x}Se$ layer. Also it should be noted that 65% of the incident laser power is absorbed into the binary selenide precursor compared to only 16% in the stacked elemental layer case. Heat flow modeling shows that although the power is dissipated in the $Cu_{2-x}Se$ phase, heat flows to the In_2Se_3 almost instantaneously (compared to the timescale of heat flow through the glass), and a maximum temperature of 923 K is reached – 100 K above the required temperature, for a 30 minute annealing (Table 1). Thus assuming the extra thermal energy increases the diffusion of the elements, CISe formation should be expected.

$CuInSe_2$ couples weakly to the irradiating beam due to its relatively lower absorption coefficient. Incomplete absorption within the 1 micron thick CISe layer leads to Fabry–Perot oscillations; the interference pattern resulting from reflection of the beam at the $CuInSe_2$/Mo interface (Fig. 2c). The total power absorbed is similar to the binary selenide stack leading to a similar maximum annealing temperature of 923 K.

To summarize the predicted interaction of the laser with each precursor, (a) the Cu/In/Se absorbs 16% of the incident power whilst (b) the binary selenide and (c) the codeposited precursors absorb 65 and 70% respectively. All precursors heat uniformly through the depth with the binary selenide and codeposited precursors achieving more than twice the temperature of the stacked elemental layer precursor. Thus it is expected that higher quality CISe is formed for the binary selenide and codeposited precursors than the stacked elemental layers.

3. Experimental laser annealing results

To evaluate the modeling predictions of Section 2, the electrodeposited precursor types characterized in Section 1 were annealed using a CW λ = 1064 nm Nd:YAG laser at 150 W cm^{-2}, rastered across the sample at a scan speed of 2 mm s^{-1}. The results of these experiments are given in Fig. 3.

A schematic is shown in Fig. 3(a) which demonstrates the changes occurring during annealing as reasoned from the measured evidence shown in (b) and (c). For stacked elemental layered precursors (Fig. 3I), the SEM micrographs show that the flat, smooth layer of Se (i) is replaced by a granular surface (ii). These grains are expected to be In_2Se_3, which is observed as the dominant phase in the XRD diffractogram of Fig. 3(Icii). In_2Se_3 is formed as a result of the high power density at the In/Se interface, as identified in the previous section, which causes strong localized heating and promotes reactions between the In and Se. Although the simulated maximum temperature is 473 K, local temperatures at the In/Se interface could be higher. 493 K is sufficient to melt and vaporize selenium whilst elemental In melts at 440 K and thus could dewet from the Cu surface. Also in the experimental samples, the In deposited as an islanded film. Either indium melting or selenium droplet formation can explain the granular surface in (ii). EDX measurements of the annealed layer reveal a Se/(Cu + In) ratio of 0.79. This means that most of the selenium was lost to the atmosphere and non-stoichiometric material can be expected. There is a low intensity peak at 26.6° 2θ visible in the annealed Cu/In/Se diffractogram which may correspond with the 112 Bragg peak of $CuInSe_2$, or Cu_2Se which also has a peak at 26.6° 2θ (JCPDS card file: 053-0523). Whilst the presence of this peak indicates that some Cu has reacted, its low intensity and the absence of additional peaks indicate the low concentration of Cu-compounds within the film. However, the diffractogram of the precursor (Fig. 3Ici) indicates that there has been some Cu–In alloy formation prior to annealing, not accounted for in the model, which may facilitate CISe formation. Overall the presence of a large amount of secondary phases, and the lack of clear evidence of CISe suggests that the sample did not reach a high enough annealing temperature to allow sufficient diffusion and reaction, in agreement with the modeling of the previous section.

The results of laser annealing binary selenide precursor stacks are shown in Fig. 3(II). Using the schematic (a) of the sample before and after laser annealing the changes in the SEM micrographs of Fig. 3(IIb) can be interpreted. The large platelets of Cu–Se which appear needle-like in the surface view SEM of the precursor (i) blur after laser annealing (ii) due to the tops of the platelets melting. Further evidence of this phenomena is given in the ESI.† This observation corresponds to the strong energy absorption localized to the surface of the $Cu_{2-x}Se$. The 3-dimensionality of the $Cu_{2-x}Se$ nanostructures, may resonantly enhance the local light absorption, but was not accounted for in the FEM. Additionally, the heat diffusion through such nanostructured

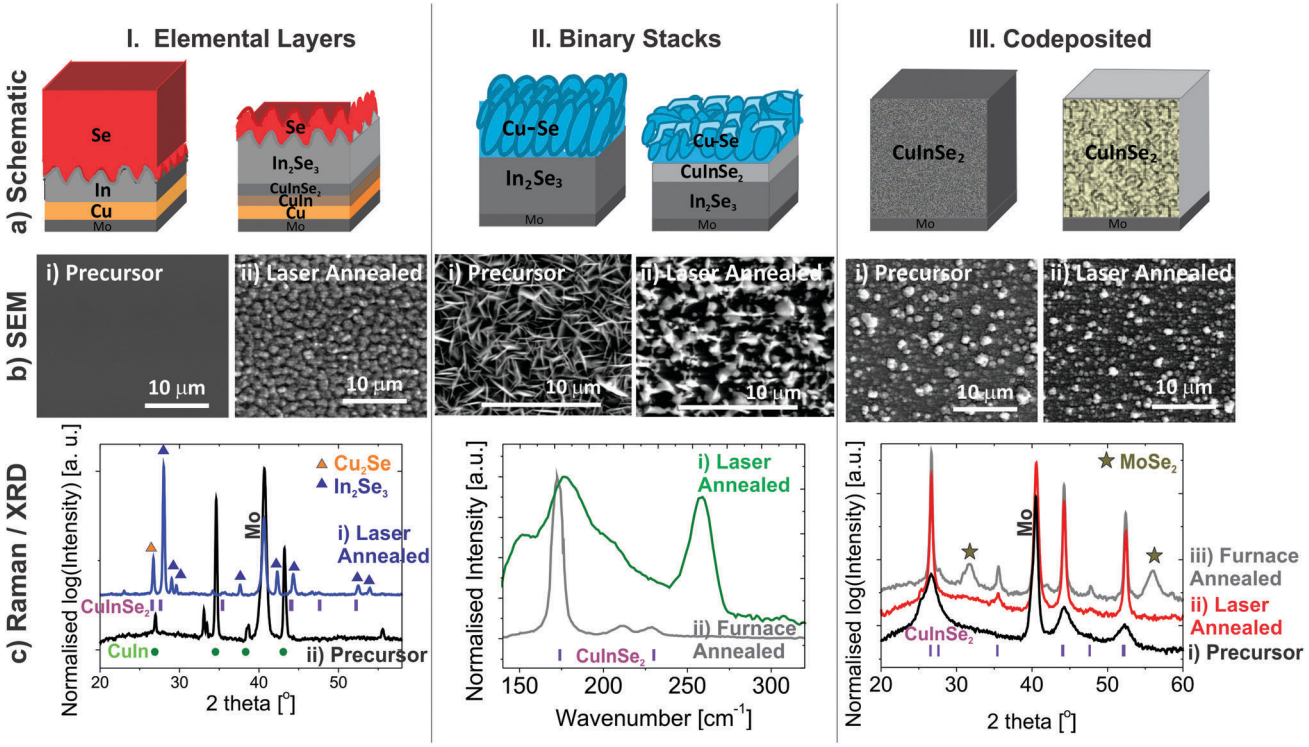

Fig. 3 (a) Schematic and (b) surface SEM of (I) elemental layers of Cu/In/Se, (II) $In_2Se_3/Cu_{2-x}Se$ binary stack and (III) coelectrodeposited $CuInSe_2$ precursor, (i) before and (ii) after laser annealing at 150 W cm^{-2}, 2 mm s^{-1}. (c) XRD diffractograms made in θ–2θ configuration of (I) and (III) of the (i) precursor and (ii) laser annealed samples. (IIc) Raman spectra of (i) laser annealed binary stack. In (c) (II) and (III) a furnace annealed coelectrodeposited absorber is shown for comparison.

and porous material will undoubtedly be lower than for the bulk material, further accentuating local heating. In order to distinguish whether CISe has formed, Raman spectroscopy is utilized due to the main modes of CISe and $Cu_{2-x}Se$ having different wavenumbers. Analyzing the Raman spectra in Fig. 3(IIc) of the laser annealed sample, $Cu_{2-x}Se$ is identified by a well-defined peak at 260 cm^{-1}.[45] There is a broad peak at similar wavenumbers to the A_1 mode of CISe (as observed clearly in the reference spectrum Fig. 3(IIcii)) but it is shifted to higher wavenumbers which may be due to a high density of defects[46] or Cu(Au) lattice ordering[47] which are both known to impair device performance. Further evidence of the lack of bulk CISe formation and a $Cu_{2-x}Se$ top surface is given by top down EDX measurement of the Cu/In ratio of 2.8, well above CISe stoichiometry, and a Se/(Cu + In) ratio of 0.75, which is well below CISe stoichiometry. It is concluded that, due to clear evidence of binary secondary phases in the SEM images and Raman spectra, that despite the model predicting an annealing temperature of 923 K, there was insufficient time to form CISe as the majority phase. A reason for slow phase formation is the nanometer sized interfacial area between the $Cu_{2-x}Se$ and the In_2Se_3. A still higher annealing temperature would be required to allow this precursor to react fully in one second.

The codeposited precursor is expected to reach a similar annealing temperature as the binary selenide stack but since most of the atoms are already near their equilibrium positions heating is only required for grain growth and removal of structural defects. The experimental results are given in Fig. 3III. There is no structural change observable in the SEM micrographs (Fig. 3IIIb) with a similar granular structure before (i) and after annealing (ii). EDX measurements show no change in Se/(Cu + In) ratio after laser annealing, maintaining a ratio of 1.04 ± 0.09. To probe the crystal structure through the depth of the film, X-ray diffractograms were measured. The broad, low intensity CISe Bragg peaks in the diffractogram of the precursor (Fig. 3IIIci), which indicate its nanocrystalline and multiphase nature, become more intense and thinner after laser annealing (ii). Determining the average apparent crystalline coherence length from the FHWM of CISe(112) peak using the Scherrer formula gives 10 ± 0.5 nm for the precursor and 118 nm after laser annealing, similar to furnace annealing.[14] The narrow symmetrical peaks of the laser annealed sample indicate no secondary phases within the CISe film at least within the resolution of the technique. A small peak at 25.5° 2θ indicates the presence of structural faults within the CISe possibly related to the very rapid cooling of the samples.[48,49]

To summarize the empirical findings; in laser annealing for 1 s, only the coelectrodeposited CISe precursor forms an absorber layer of nanocrystalline CISe with minimal quantities of secondary phases and stoichiometric amounts of selenium as required for solar cell fabrication. In contrast, the open morphology of the $Cu_{2-x}Se$ of the binary stacks and the low temperatures combined with Se loss in the elemental layer precursors both exacerbated by the short dwell times impede the diffusion and reaction required for CISe phase formation.

The large quantities of secondary phases present in these resultant two absorber layers render them unsuitable for completion into photovoltaic devices.

4. Device fabrication

In order to benchmark the power conversion efficiency of the laser annealed codeposited samples, photovoltaic devices were fabricated by etching them in KCN to remove any surface $Cu_{2-x}Se$ phases and standard buffer and window layers were deposited on top. Some codeposited precursors were laser annealed as above, while for others an elevated partial pressure of selenium of approximately 200×10^{-6} Pa (compared to the normal 1×10^{-6} Pa) was maintained during annealing. Previously, we have shown that elevated selenium partial pressure above the sample correlates with increased photoluminescence yield, which is positively correlated to the expected maximum device output voltage.[15] Grazing incidence X-ray diffraction (GIXRD) and SEM images of the precursor, samples $P_{Se}1$ and $P_{Se}200$ (the numbers refer to the vapor pressure of selenium above the samples during annealing in μPa) are shown in Fig. 4.

In Fig. 4(a) the diffractogram of the precursor shows broad and asymmetric peaks relating to the $CuInSe_2$ phase consistent with the data already shown in Fig. 3(IIIci). Laser annealing results in a narrowing of the FWHM of the major peaks of the chalcopyrite phase for both samples annealed under different P_{Se}. Comparing these diffractograms, the absorber annealed under the highest P_{Se}, $P_{Se}200$, gives narrower Bragg-peaks than $P_{Se}1$ and additionally shows the presence of minor diffraction peaks (*i.e.* 211 reflection at 35.4° 2θ) absent from the $P_{Se}1$ diffractogram. Examination of the normalized 112 peak (Fig. 4b) confirms the FWHM of $P_{Se}200$ is smaller than for $P_{Se}1$ and crystallite domains of 175 ± 3 nm and 60 ± 1 nm are calculated respectively. Both are larger than the 10 ± 1 nm calculated for the precursor. The change in crystal coherence length is consistent with our previous observations[15] and the increase in grain size directly observed by SEM cross sectional micrographs of the films (Fig. 4c). Whilst there is little change between the fine-grained structure of the precursor and $P_{Se}1$, $P_{Se}200$ exhibits large, faceted grains with dimensions between 100–300 nm. As $P_{Se}1$ and $P_{Se}200$ were from identical precursors and annealed for the same time with the same laser power, the crystallization of absorber layers, at least on the timescale of seconds, is mediated by the P_{Se} above the film. The illuminated *JV* characteristics of codeposited samples $P_{Se}1$ and $P_{Se}200$ are shown in Fig. 5a).

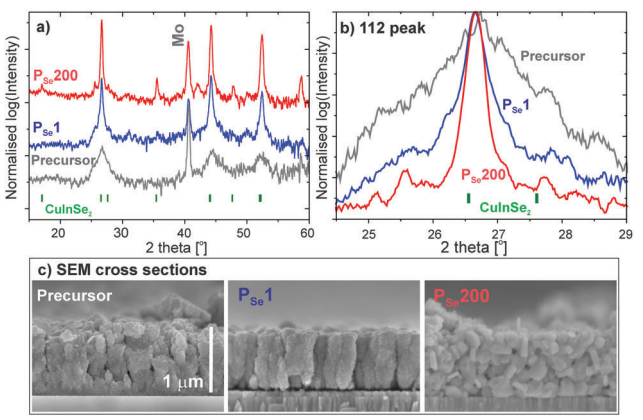

Fig. 4 (a) GIXRD diffractograms (θ = 0.75°), (b) zoom of 112 reflection and (c) SEM cross sectional micrographs of (i) a Se capped precursor (grey), and after laser annealing this precursor at 150 W cm^{-2}, 2 mm s^{-1}, (ii) sample $P_{Se}1$ (blue) and (iii) $P_{Se}200$ (red). All the SEM images are shown at the same magnification.

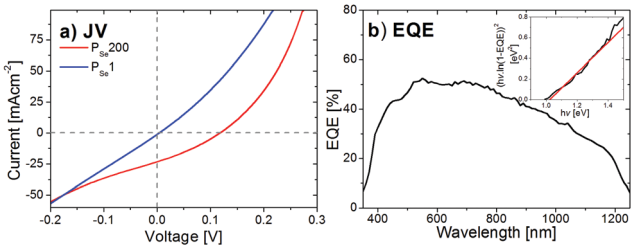

Fig. 5 (a) Illuminated current–voltage (*JV*) curves of devices fabricated from Se capped, laser annealed absorber layers: $P_{Se}1$ (blue) and $P_{Se}200$ (red). (b) EQE spectrum of the $P_{Se}200$ device with the red line of the inset graph showing the extrapolated band gap.

$P_{Se}1$, the sample annealed without an extra partial pressure of selenium, behaves like a resistor with no power conversion efficiency. However, the four devices constructed from $P_{Se}200$ all produced working solar cells with a best efficiency of 1.6% and an average efficiency of 1.2%. Although this efficiency is very low compared to other absorber fabrication techniques, it should be noted that the annealing step has been reduced to the order of seconds in this case. The best device had an open circuit voltage, V_{oc}, of 0.194 V, a short circuit current density, J_{sc}, of 23.0 mA cm^{-2}, a fill factor of 37%, a shunt resistance of 20 Ω cm^2 and a series resistance of 6 Ω cm^2. For comparison, the V_{oc} of world record CISe devices are two and a half times higher, and the J_{sc} is almost doubled that found here.[50] Efficient CISe devices normally have a shunt resistance of at least one order of magnitude higher and series resistances of about one order of magnitude lower. The external quantum efficiency (EQE) spectrum of a $P_{Se}200$ device is shown in Fig. 5b. The current collection is low across the entire wavelength range with a maximum EQE of 52%. The long wavelength region of the EQE was analyzed to find the band gap of the CISe absorber layer. Gärtner showed that the EQE could be expressed as

$$\mathrm{EQE} = 1 - \frac{\exp(-\alpha W)}{1 + \alpha L} \qquad (3)$$

where α is the wavelength dependent absorption co-efficient, W is the space charge width and L is the minority carrier diffusion length.[51] When the diffusion length is small eqn (3) reduces to

$$\mathrm{EQE} = 1 - \exp(-\alpha W) \qquad (4)$$

CISe is a direct band gap semiconductor and should therefore follow the relationship $\alpha h\nu \propto (h\nu - E_g)^{1/2}$ where $h\nu$ is the photon energy and E_g is the band gap. Plotting $(\alpha h\nu)^2$ against

photon energy allows the band gap to be estimated. In this case α is obtained from rearranging eqn (4). The inset of Fig. 5b shows this plot and the extrapolated band gap is found to be 1.02 $\pm$ 0.04 eV consistent with literature values for stoichiometric CISe.[50] The integral of the AM 1.5 spectrum with the EQE gives a short circuit current of 20.9 mA cm^{-2}, which is lower than that measured by the *JV* curve (Fig. 4a). One reason for this is that the current collection within the cell is spatially non-uniform, which is likely related to the non-uniform thermal history induced by the Gaussian shape and the rastering of the laser beam over the surface.[27] Heat flow modeling of two passes of a rastered laser show that material on the edges of the beam only reaches a maximum temperature of 673 K (see ESI†) which is normally insufficient for high quality CISe material. Experimental evidence for the non-uniform heating is shown by the striped appearance of the samples after laser annealing, which qualitatively matches the patterns of the heat flow model (see ESI†). The performance of a whole cell is detrimentally affected by the presence of lateral variations in absorber layer material quality, which can thus begin to explain the poor performance observed here.[52,53]

Conclusions

In this work, the structural and optical properties of three different electrodeposited CISe precursors have been considered in order to determine their applicability for next-generation rapid annealing by lamps or lasers to achieve high-throughput manufacturing. Using finite element modeling, the dissipation of the laser power through each precursor stack and the resulting temperature profiles were calculated. From these profiles the most suitable precursor structures for transient laser annealing were predicted to be either the codeposited CISe or the binary stack of $In_2Se_3/Cu_{2-x}Se$ due to the sufficient annealing temperatures in contrast to the stacked elemental layers. This prediction was partially supported empirically, as the codeposited CISe lead to nanocrystalline CISe whilst the binary stack did not. For the codeposited structure the elements only had to move to their equilibrium positions which was possible with the available thermal energy and time, whilst the open, voided morphology of the binary selenide stack resulting from the electrodeposition hindered diffusion and reaction required for complete CISe formation. The stacked elemental layer sample, despite being compact, did not form a majority phase of CISe during annealing since it did not achieve a high annealing temperature and selenium was lost to the vapor phase. Laser processing of codeposited precursors into device-suitable absorber layers has been demonstrated by fabrication of functioning devices (albeit of low efficiency). Key to future improvements will be achieving lateral uniformity in temperature-time profiles which will result in uniform CISe properties and the use of elevated selenium partial pressure. More detailed absorber layer and device characterization is required in order to fully understand the constraints of the current process and point the direction for further improvement.

Acknowledgements

The authors thank the reviewers for their input in improving the manuscript. The work in Luxembourg was supported by Fonds National de la Recherche du Luxembourg grant MAT09/02. In Utah, the work on $CuInSe_2$ experiments was supported by the US National Science Foundation under the Materials World Network award 1008302 while the work on modeling was supported by the US Department of Energy *via* the Bay Area Photovoltaic Consortium under prime award DE-EE0004946. The authors would like to thank and recognize the help of Maxime Thevenin for EDX/SEM, Institut de Recherche et Développement sur l'Energie Photvoltaique for cell completion, *JV*, and EQE measurements, and Cédric Broussillou for helpful discussions. This is an official contribution of NIST; not subject to copyright. Description of commercial products herein is for information only; it does not imply recommendation or endorsement by NIST.

Notes and references

1 https://www.zsw-bw.de/fileadmin/user_upload/PDFs/Pressemitteilungen/2016/pr09-2016-ZSW-WorldRecordCIGS.pdf.
2 K. Kushiya, A. Shimizu, K. Saito, A. Yamada and M. Konagai, Development of high-efficiency $CuIn_xGa_{1-x}Se_2$ thin-film solar cells by selenization with elemental Se vapor in vacuum, *Proceedings of 1994 IEEE 1st World Conference on Photovoltaic Energy Conversion - WCPEC (A Joint Conference of PVSC, PVSEC and PSEC)*, Waikoloa, HI, 1994, vol. 1, pp. 87–90.
3 K. Kim, G. M. Hanket, H. Trang and W. N. Shafarman, *J. Appl. Phys.*, 2012, **111**, 083710.
4 Y. E. Romanyuk, H. Hagendorfer, P. Stuecheli, P. Fuchs, A. R. Uhl, C. M. Sutter-Fella, M. Werner, S. Haass, J. Stueckelberger, C. Broussillou, P.-P. Grand, V. Bermudez and A. N. Tiwari, *Adv. Funct. Mater.*, 2015, **25**, 12–27.
5 M. Weizman, H. Rhein, J. Dore, S. Gall, C. Klimm, G. Andrae, C. Schultz, F. Fink, B. Rau and R. Schlatmann, *Sol. Energy Mater. Sol. Cells*, 2014, **120**, 521–525.
6 G. Mincuzzi, M. Schulz-Ruhtenberg, L. Vesce, A. Reale, A. Di Carlo, A. Gillner and T. M. Brown, *Prog. Photovoltaics*, 2014, **22**, 308–317.
7 X. Wang, S. S. Li, C. H. Huang, S. Rawal, J. M. Howard, V. Craciun, T. J. Anderson and O. D. Crisalle, *Sol. Energy Mater. Sol. Cells*, 2005, **88**, 65–73.
8 M. Nakamura, N. Yoneyama, K. Horiguchi, Y. Iwata, K. Yamaguchi, H. Sugimoto and T. Kato, Recent R&D progress in solar frontier's small-sized Cu(InGa)(SeS)2 solar cells, *2014 IEEE 40th Photovoltaic Specialist Conference (PVSC)*, Denver, CO, 2014, pp. 0107–0110.
9 S. R. Dhage, M. Tak and S. V. Joshi, *Mater. Lett.*, 2014, **134**, 302–305.
10 M. C. Joliet, C. Antoniadis, R. Andrew and L. D. Laude, *Appl. Phys. Lett.*, 1985, **46**, 266–267.
11 L. D. Laude, M. C. Joliet and C. Antoniadis, *Sol. Cells*, 1986, **16**, 199–209.

12 D. Bhattacharyya, S. Bocking and M. J. Carter, *J. Mater. Sci.*, 1996, **31**, 5451–5456.
13 S. Jost, R. Schurr, F. Hergert, R. Hock, J. Schulze, A. Kirbs, T. Voß, M. Purwins, J. Palm and I. Mys, *Sol. Energy Mater. Sol. Cells*, 2008, **92**, 410–417.
14 H. J. Meadows, A. Bhatia, V. Depredurand, J. Guillot, D. Regesch, A. Malyeyev, D. Colombara, M. A. Scarpulla, S. Siebentritt and P. J. Dale, *J. Phys. Chem. C*, 2013, **118**, 1451–1460.
15 H. J. Meadows, D. Regesch, T. Schuler, S. Misra, B. J. Simonds, M. A. Scarpulla, V. Gerliz, L. Gutay and P. Dale, The importance of Se partial pressure in the laser annealing of CuInSe2 electrodeposited precursors, *2014 IEEE 40th Photovoltaic Specialist Conference (PVSC)*, Denver, CO, 2014, pp. 0405–0408.
16 C. J. Stolle, T. B. Harvey, D. R. Pernik, J. I. Hibbert, J. Du, D. J. Rhee, V. A. Akhavan, R. D. Schaller and B. A. Korgel, *J. Phys. Chem. Lett.*, 2014, **5**, 304–309.
17 A. Chirila, P. Reinhard, F. Pianezzi, P. Bloesch, A. R. Uhl, C. Fella, L. Kranz, D. Keller, C. Gretener, H. Hagendorfer, D. Jaeger, R. Erni, S. Nishiwaki, S. Buecheler and A. N. Tiwari, *Nat. Mater.*, 2013, **12**, 1107–1111.
18 J. Fischer, S. Siebentritt and P. Dale, *ECS Trans.*, 2010, **25**, 129–142.
19 A. Kampmann, J. Rechid, A. Raitzig, S. Wulff, R. Mihhailova, R. Thyen and K. Kalberlah, *Proceeding of the MRS Sprin Meeting*, San Francisco, 2003.
20 J. F. Guillemoles, *Thin Solid Films*, 2000, **361**, 338–345.
21 J. J. Scragg, P. J. Dale, D. Colombara and L. M. Peter, *ChemPhysChem*, 2012, **13**, 3035–3046.
22 F. Hergert, S. Jost, R. Hock, M. Purwins and J. Palm, *Thin Solid Films*, 2007, **515**, 5843–5847.
23 J. F. Guillemoles, A. Lusson, P. Cowache, S. Massaccesi, J. Vedel and D. Lincot, *Adv. Mater.*, 1994, **6**, 376–379.
24 J. J. Scragg, D. M. Berg and P. J. Dale, *J. Electroanal. Chem.*, 2010, **646**, 52–59.
25 E. Rusli, F. Xue, T. O. Drews, P. M. Vereecken, P. Andricacos, H. Deligianni, R. D. Braatz and R. C. Alkire, *J. Electrochem. Soc.*, 2007, **154**, D584–D597.
26 J. Fischer, J. K. Larsen, J. Guillot, Y. Aida, T. Eisenbarth, D. Regesch, V. Depredurand, N. Fevre, S. Siebentritt and P. J. Dale, *Sol. Energy Mater. Sol. Cells*, 2014, **126**, 88–95.
27 H. J. Meadows, D. Regesch, M. Thevenin, J. Sendler, T. Schuler, S. Misra, B. J. Simonds, M. A. Scarpulla, V. Gerliz, L. Guetay, J. Guillot and P. J. Dale, *Thin Solid Films*, 2015, **582**, 23–26.
28 M. A. Ordal, R. J. Bell, R. W. Alexander, L. A. Newquist and M. R. Querry, *Appl. Opt.*, 1988, **27**, 1203–1208.
29 L. Gampel and F. M. Johnson, *J. Opt. Soc. Am.*, 1969, **59**, 72–73.
30 A. I. Golovashkin, I. S. Levchenko, G. P. Motulevich and A. A. Shubin, *Zh. Eksp. Teor. Fiz.*, 1966, **51**, 1622 (*Sov. Phys. JETP*, 1967, **24**, 1093).
31 A. D. Rakic, A. B. Djurisic, J. M. Elazar and M. L. Majewski, *Appl. Opt.*, 1998, **37**, 5271–5283.
32 H. T. Elshair and A. E. Bekheet, *J. Phys. D: Appl. Phys.*, 1992, **25**, 1122–1130.
33 N. Okereke and A. Ekpunobi, *Res. J. Chem. Sci.*, 2011, **2231**, 606X.
34 M. I. Alonso, K. Wakita, J. Pascual, M. Garriga and N. Yamamoto, *Phys. Rev. B: Condens. Matter Mater. Phys.*, 2001, **63**, 075203.
35 *CRC Handbook of Chemistry and Physics*, ed. R. D. Lide, CRC Press, Boca Raton, 84th edn, 2003.
36 L. Gulay, M. Daszkiewicz, O. Strok and A. Pietraszko, *Chem. Met. Alloys*, 2011, **4**, 200–205.
37 O. Madelung, *Semiconductors*, Springer, Berlin – Heidelberg, 3rd edn, 2004.
38 *Lange's Handbook of Chemistry*, ed. J. A. Dean, Section 4, Table 4.1, Electronic Configuration and Properties of the Elements, McGraw-Hill, 15th edn, 1999.
39 M. Böhm, O. Madelung, G. Huber, A. MacKinnon, A. Scharmann and E. G. Scharmer, *Landolt-Boernstein Numerical Data and Functional Relationships in Science and Technology*, Group III, Semiconductors, Subvolume H Physics of Ternary Compounds, Springer, Berlin, 1985, vol. 17, p. 337.
40 X. Su, F. Fu, Y. Yan, G. Zheng, T. Liang, Q. Zhang, X. Cheng, D. Yang, H. Chi, X. Tang, Q. Zhang and C. Uher, *Nat. Commun.*, 2014, **5**, 4908.
41 A. Rockett and R. W. Birkmire, *J. Appl. Phys.*, 1991, **70**, R81–R97.
42 U. Gaur, H. C. Shu, A. Mehta and B. Wunderlich, *J. Phys. Chem. Ref. Data*, 1981, **10**, 89–117.
43 T. J. Anderson, O. D. Crisalle, S. S. Li and P. H. Holloway, *Future CIS Manufacturing Technology Development, Final Report*, NREL, 2003.
44 A. Bhatia, H. Meadows, A. Crossay, P. J. Dale and M. A. Scarpulla, *J. Appl. Phys.*, 2013, **114**, 044904.
45 X. Fontane, V. Izquierdo-Roca, L. Calvo-Barrio, J. Alvarez-Garcia, A. Perez-Rodriguez, J. R. Morante and W. Witte, *Appl. Phys. Lett.*, 2009, **95**, 121907.
46 C. M. Ruiz, X. Fontane, A. Fairbrother, V. Izquierdo-Roca, C. Broussillou, S. Bodnar, A. Perez-Rodriguez and V. Bermudez, *Appl. Phys. Lett.*, 2013, **102**, 091106.
47 C. Xu, H. Li, X. Ye and M. Chen, in *Proceedings of ISES World Congress 2007*, ed. D. Y. Goswami and Y. Zhao, Springer Berlin Heidelberg, 2009, ch. 259, vol. I–V, pp. 1285–1288.
48 H. Rodriguez-Alvarez, N. Barreau, C. A. Kaufmann, A. Weber, M. Klaus, T. Painchaud, H. W. Schock and R. Mainz, *Acta Mater.*, 2014, **79**, 436.
49 H. J. Meadows, A. Bhatia, C. Stefan, S. Schorr, M. A. Scarpulla and P. J. Dale, *Thin Film Solar Technology V*, 2013, vol. 8823.
50 J. A. M. AbuShama, S. Johnston, T. Moriarty, G. Teeter, K. Ramanathan and R. Noufi, *Prog. Photovoltaics*, 2004, **12**, 39–45.
51 W. W. Gärtner, *Phys. Rev.*, 1959, **116**, 84–87.
52 U. Rau, P. O. Grabitz and J. H. Werner, *Appl. Phys. Lett.*, 2004, **85**, 6010–6012.
53 P. O. Grabitz, U. Rau and J. H. Werner, *Phys. Status Solidi A*, 2005, **202**, 2920–2927.

